

Redox-Dependent Franck–Condon Blockade and Avalanche Transport in a Graphene–Fullerene Single-Molecule Transistor

Chit Siong Lau,[†] Hatef Sadeghi,[‡] Gregory Rogers,[†] Sara Sangtarash,[‡] Panagiotis Dallas,[†] Kyriakos Porfyraakis,[†] Jamie Warner,[†] Colin J. Lambert,[‡] G. Andrew D. Briggs,[†] and Jan A. Mol*^{‡,†}

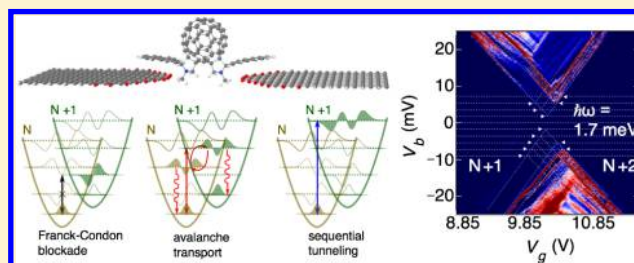
[†]Department of Materials, University of Oxford, 16 Parks Road, Oxford OX1 3PH, United Kingdom

[‡]Quantum Technology Center, Physics Department, Lancaster University, Lancaster LA1 4YB, United Kingdom

Supporting Information

ABSTRACT: We report transport measurements on a graphene–fullerene single-molecule transistor. The device architecture where a functionalized C₆₀ binds to graphene nanoelectrodes results in strong electron–vibron coupling and weak vibron relaxation. Using a combined approach of transport spectroscopy, Raman spectroscopy, and DFT calculations, we demonstrate center-of-mass oscillations, redox-dependent Franck–Condon blockade, and a transport regime characterized by avalanche tunnelling in a single-molecule transistor.

KEYWORDS: Single-molecule electronics, Franck–Condon blockade, avalanche transport, electron–vibron coupling, graphene



Coupling between electronic and vibrational degrees of freedom in single-molecule devices can lead to transport properties very different from those of metal/semiconductor nanostructures.¹ Charge transfer can excite vibrational modes,² or vibrons, and strong electron–vibron coupling leads to suppression of tunnel current at low bias.^{3,4} Theory further predicts super-Poissonian current noise, characterized by giant Fano factors, for molecular junctions with weak vibron-relaxation owing to avalanche-type charge transfer.⁵ Here, we demonstrate a device architecture of a single-molecule transistor where a functionalized C₆₀ binds to graphene nanoelectrodes via π – π interactions. The stability and weak vibron-relaxation of our system enables us to investigate redox-dependent electron–vibron coupling and avalanche transport.

We perform transport measurements of graphene–fullerene single-molecule transistors fabricated using feedback-controlled electroburning.⁶ The molecule bridging the graphene nanogap is a pyrene functionalized C₆₀ bisadduct synthesized through a 1,3 dipolar cycloaddition using 1-pyrene carboxaldehyde and N-methylglycine (Supporting Information Section 1.1).⁷ While the functionalization results in different isomers, steric considerations mean only the cis-2 and cis-3 isomers are expected to bridge the graphene nanogap. Density functional theory (DFT) calculations of the relaxed graphene–fullerene–graphene structure confirm that the cis-3 isomer forms the most stable configuration without steric hindrance, as shown in Figure 1a. Iso-surfaces of the frontier orbitals of gas phase cis-3 isomer are shown in Figure 1b.⁸ The wave function of the lowest unoccupied molecular orbital (LUMO) level is mostly localized in the central C₆₀, whereas for the highest occupied molecular orbital (HOMO) level, the wave function is extended to the pyrene anchors. Comparison of the iso-surfaces of frontier orbitals for cis-2 and cis-3 isomers further show that the

wave function delocalization of the HOMO levels are more pronounced in the cis-3 isomer, indicating that it has a better π – π interaction with the graphene electrodes and is therefore more likely to bridge the junction (Supporting Information Figure S12). In pristine C₆₀, DFT predicts LUMO dominated transport that was verified with thermoelectric experiments.⁹ In contrast, our DFT calculations predict that charge transport in the bisadduct is more likely to be HOMO dominated.^{10,11}

Figure 1c shows the current I as a function of bias V_b and gate voltage V_g of a single-molecule transistor (device A), measured at 20 mK. The addition energies between adjacent redox states, measured from the height of the Coulomb diamonds, are $E_{\text{add}} \sim 160$ meV for all charge-state transitions. We attribute the absence of odd/even oscillations of E_{add} , previously observed for two-fold spin shell systems,^{6,12} to orbital degeneracies of the C₆₀ molecule.¹³ Calculations have shown that the interactions within each shell in C₆₀ are almost constant with only a slight increase of the electron–electron on-site Coulomb interaction in the middle of each shell where electrons with opposite spins begin to fill.¹³ We observe a small increase of ~ 10 meV per electron added from charge state N to $N + 2$ which we attribute to the on-site Coulomb interactions. In the constant interaction model E_{add} is given by the sum of the charging energy E_C , due to Coulomb interactions of the electrons in the molecule, and the energy gap Δ_{HL} between the HOMO and LUMO.¹⁴ For a two-fold degenerate system, E_{add} oscillates between E_C and $E_C + \Delta_{\text{HL}}$, while for systems with higher degeneracies, $E_{\text{add}} = E_C$ until a level is completely filled.

Received: August 26, 2015

Revised: December 2, 2015

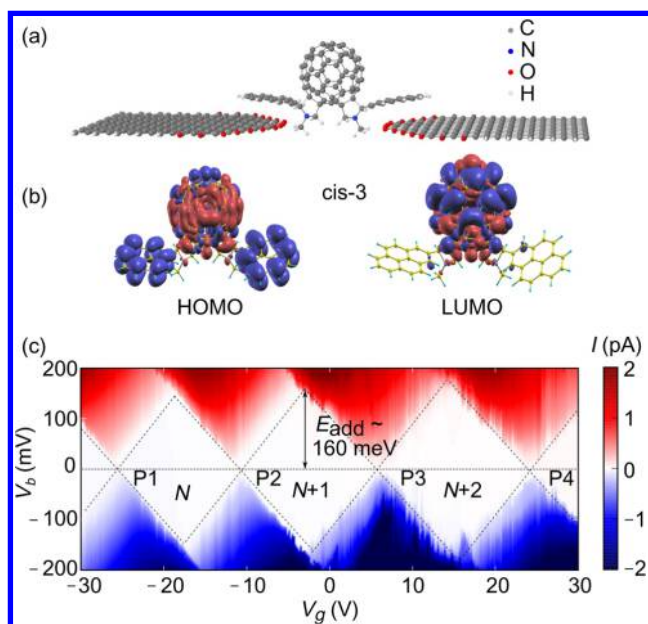


Figure 1. (a) DFT calculations showing the relaxed structure of the cis-3 isomer bridging the graphene nanogap. The electrodes are fabricated using feedback-controlled electroburning of chemical vapor deposition grown graphene transferred to a heavily doped silicon substrate with a 300 nm thick silicon oxide layer, which also serves as a back-gate that electrostatically modulates the chemical potential of the molecule. The molecules are deposited on the electrodes from a chloroform solution (Methods). (b) DFT simulations of the iso-surfaces of the LUMO and HOMO of cis-3 isomer. (c) Current stability diagram of device A. All measurements are performed at 20 mK unless otherwise stated. Within each diamond, the system is in Coulomb blockade and the charge on the molecule is stable. The molecular redox state changes by one between adjacent diamonds.

From the fact that E_{add} here is constant for three charge-state transitions, we infer that electrons are filling exclusively an orbital that is at least four-fold degenerate. We conclude that charge transport is HOMO dominated based on two independent observations: (i) DFT calculations predict that the Fermi energy of the graphene leads are closer aligned to the HOMO than to the LUMO and, (ii) the experimentally observed level degeneracy is compared to DFT calculations of the Kohn–Sham energy levels, which indicate that the HOMO (-4.59 eV) and HOMO-1 (-4.60 eV) are nearly degenerate whereas the LUMO (-3.12 eV) and LUMO+1 (-2.86 eV) are well separated in energy (Supporting Information Section 2.3).

Figure 2 shows a map of the differential conductance G of charge transition $N + 1$ to $N + 2$ of device A taken with a higher resolution (P3 in Figure 1c). The gate potential for the charge transition is different for repeated measurements due to a common hysteretic effect likely related to charge traps in the oxide. The effect occurs when the gate potential is swept quickly across a large range but is otherwise stable when swept slowly. We observe lines corresponding to excited state transitions at energies ≥ 33 meV (white arrows) that are in excellent agreement with the intrinsic vibrational modes of pristine C_{60} ,¹⁵ as summarized in Table 1. We also observe excited states at energies < 33 meV (green arrows), below the lowest vibrational mode of the pristine C_{60} . The asymmetry of the excited states on the bias polarity can be explained through a rate equation model involving asymmetric tunnelling barriers, which was previously observed in the orbital excited state

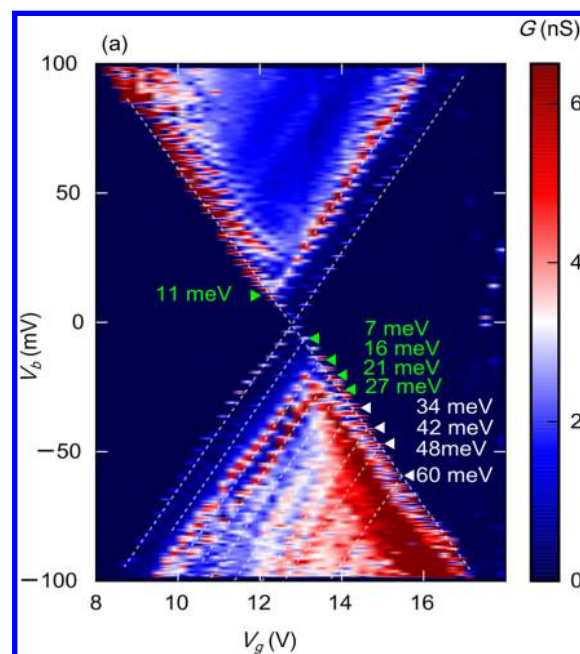


Figure 2. (a) Conductance stability diagram of the $N + 1$ to $N + 2$ transition (P3 in Figure 1c) obtained by taking the numerical derivative of the current measured. Excited states are indicated by the white and green arrows. Details on how the excited states are determined are included in Supporting Information Section 1.5.

Table 1. Comparison between Measured Excitation Energies from Transport and Raman Spectroscopy, Calculated Values and Intrinsic Vibrational Modes of Pristine C_{60} ^a

mode	energy (meV)			
	transport (this work)	Raman (this work)	DFT (this work)	DFT (pristine C_{60}) (ref 15)
CM T_y	7		8	
CM T_x			10	
CM R_z	11	13	12	
CM T_z	16	16	16	
CM R_x	21	19	19	
CM R_y	27	25	21	
$H_g(1)$	34	33	32, 33, 34	33
$T_{2u}(1)$	42			43
$G_u(1)$	42			43
$H_g(2)$	48	55		53
$A_g(1)$	60	61		61

^aTransport measurements are performed at 20 mK in vacuum with the molecule anchored to graphene electrodes. Raman spectroscopy is performed at room temperature with the molecules drop-casted on to gold-coated silicon/glass substrates to enhance the Raman scattering. DFT calculations are performed with the condition where the degrees of motion of the anchor groups are completely restricted in order to elucidate the center-of-mass (CM) motions. In the actual system, the pyrene groups are expected to exhibit small motions. The values for the vibrational modes of pristine C_{60} are obtained from ref 15. We find that the discrepancies between our measurements fall within the range of values reported in ref 18, which are obtained from experiments and ab initio theories reported by different groups and can differ by up to 10 meV.

spectrum of a single donor in silicon. When the excited state relaxations are fast compared to the tunneling rates, an electron can tunnel on to the molecule through any number of excited states that lie within the bias window but only leave through the

ground state as the molecule relaxes. In the limit where the molecule-electrodes coupling is very asymmetric, current steps are not expected for one bias polarity.¹⁶

A comparison of the transport spectroscopy and Raman spectra of pristine C₆₀ and bisadduct (Table 1) indicates that these excited state transitions have a vibrational nature. To identify the mechanical motion of these additional low-lying vibrational modes, we use DFT results where we analyze the mechanical degrees of freedom of the bisadduct in the limit where the atomic mass of the pyrene anchor groups approach infinity (Supporting Information Section 2.6). In this limit, the anchor groups are effectively clamped and the modes corresponding to internal vibrations of the pyrene are filtered from the vibrational spectrum. DFT calculations in this limit reveal six vibrational modes at energies <33 meV with two sets of three modes each corresponding to the translational and rotational center-of-mass (CM) motion of the central C₆₀ with respect to the anchor groups (Figure S14a, animations in Supporting Information).

Figure 3 shows low energy excitations observed for all four charge transitions (P1–4 in Figure 1c) with spacings of 1.7

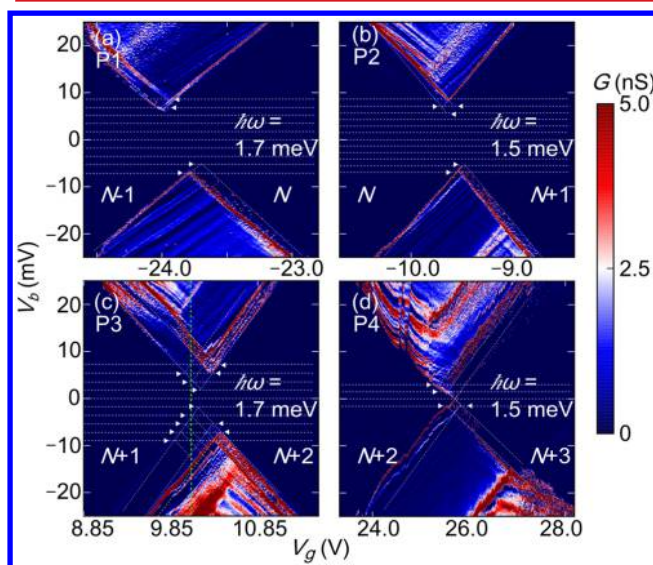


Figure 3. (a–d) Conductance stability diagrams for transitions $N - 1$ to $N + 3$. The low bias current suppression is due to FC blockade in systems with strong electron-vibron coupling. Sets of integer spaced vibrational state lines (white arrows) are observed in the low bias regime. The vertical green line in (c) is the gate voltage at which the large current noise discussed in Figure 5 is measured. The energy of a single vibrational quantum, $\hbar\omega$, is extracted for all four charge transitions (Supporting Information Section 1.5).

meV (P1), 1.5 meV (P2), 1.7 meV (P3), and 1.5 meV (P4) (white arrows). Low energy excitations are similarly observed in measurements of device B (~ 2 meV, Supporting Information Figure S8a). Lines with different slopes, corresponding to different capacitive couplings, are probably not related to the energy spectrum of the molecule. They can be from a different Coulomb diamond related to a separate quantum dot located close to the device or associated with density of states fluctuations in the graphene electrodes. Similar fluctuations have also been observed in silicon SETs.¹⁷ To account for the nature of the low energy excitations (~ 2 meV), we analyze the vibrational modes of the bisadduct using DFT where all the mechanical degrees of freedom of the atoms are allowed

(Supporting Information Section 2.6). The lowest nonzero mode is at 1.7 meV, consistent with our measurements (Supporting Information Figure S14b). This mode is due to the combined center-of-mass motions of the central C₆₀ and pyrene anchors moving perpendicularly relative to each other with the central C₆₀ moving out-of-plane while the anchors move in-plane (animation in Supporting Information). Our findings are consistent with a previous report that the binding energy of pyrene to graphene is much stronger out-of-plane compared to in-plane, such that the pyrene anchors can more easily slide on the graphene electrodes.¹⁸

The Coulomb diamond edges do not intersect at zero bias for P1–3 (Figure 3a–c) and in device C (Supporting Information Figure S8b). The current suppression at low bias remain unchanged with the application of a magnetic field, ruling out a magnetic origin (Supporting Information Figure S7)¹⁹ and the size of the gaps correspond to an integer spacing of the energy excitations. We attribute these features to Franck–Condon (FC) blockade that occurs for strong electron-vibron coupling,⁵ illustrated in Figure 5a. Electrons tunnelling onto the molecule shifts the equilibrium coordinates of the harmonic oscillator wave functions for charge states N and $N + 1$ by an amount proportional to the dimensionless electron-vibron coupling constant λ . For strong coupling, $\lambda \gg 1$, the equilibrium coordinates of the $N + 1$ charge state is greatly displaced from that of the N charge state (Figure 5a). As a result, the transition rate between the vibronic ground states of charge states N and $N + 1$, determined by the overlap of the vibron wave functions, is exponentially reduced with λ , leading to current suppression at low bias. The FC blockade is lifted when the applied bias is sufficiently large for transitions from the vibronic ground state to higher excited states (Figure 5c), where the transition rates are higher from increased overlap of the vibronic wave functions. When electrons are added to the molecule, we observe a decrease of the FC gap from P2 to P4, such that for P4 (Figure 3d), the FC blockade is completely lifted. The FC gap, that is, the threshold voltage at which the FC blockade is lifted when it matches a multiple of the vibrational quantum $n\hbar\omega$, is proportional to $\lambda^2 \hbar\omega$.⁵ Additional electrons on the molecule shift the equilibrium positions of the harmonic oscillator wave functions, leading to a smaller displacement of the equilibrium coordinates between charge states $N + 2$ and $N + 3$, that is, a smaller λ . The higher transition rate for the vibronic ground states from the increased wave function overlap allows for current in the previously FC blockade region. Redox-dependent electron-vibron coupling is possibly due to Jahn–Teller (JT) distortion of the molecule,²⁰ which is particularly strong in molecules with a large orbital degeneracy and high spatial symmetry such as C₆₀.²¹ The geometrical JT distortion lowers the overall ground state energy, which is directly proportional to λ , as derived in ref 23. Our observation of HOMO degeneracy and a charge state dependent λ is in line with these predictions.

Using the set of evenly spaced excitations of P3 (Figure 3c) and fitting them to the rate equation model,²² we determine $\lambda = 3.0$ for the charge transition $N + 1$ to $N + 2$ (Supporting Information Section 1.5). We simulate the stability diagram for an asymmetric molecule-electrode tunnel coupling, dependent on the contact geometry of the molecule to the electrodes, $t_L = 0.2t_R$ (Figure 4b), which shows good qualitative agreement with our measurements (Figure 4a). The electroburnt graphene nanoelectrodes are not likely to be symmetric on the atomic scale, which can lead to asymmetric positioning of the molecule

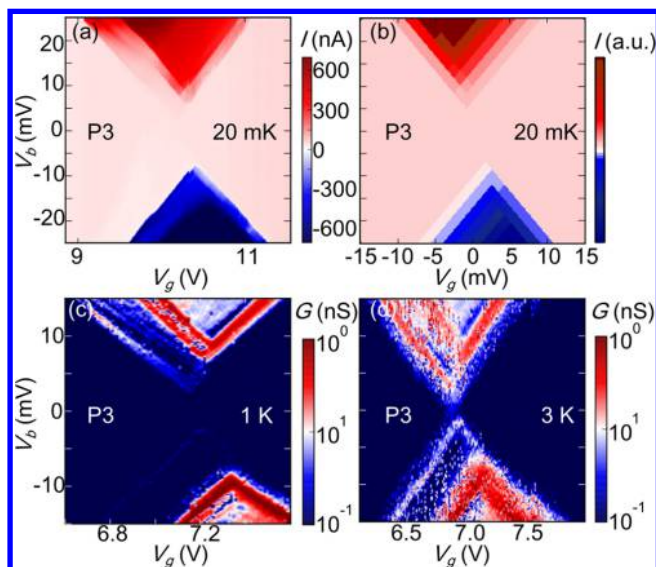


Figure 4. (a) Current stability diagram of P3 at 20 mK. (b) Simulated current stability diagram using the rate equation model with $\lambda = 3$ and $t_L = 0.2t_R$, showing good qualitative agreement with (a). Conductance stability diagrams of P3 at 1 K (c) and 3 K (d). The FC gap is lifted at 3 K. Transitions due to vibron absorption are described by Bose–Einstein statistics, such that $I_{\text{step}} \propto 1/k_B T \times 1/(\exp(\hbar\omega/k_B T) - 1)$. We extract and fit the temperature dependence of I at $V_g = 7$ V and $V_b = 7.2$ mV in Figure 3c and obtained a value of $\hbar\omega = 1.7$ meV, consistent with our experimentally determined value.

across the junction. Furthermore, our DFT calculations show that the pyrene anchors are not symmetric relative to the central C_{60} (Supporting Information Section 2.2).

At elevated temperatures, T , the thermal equilibrium population of vibrational excited states with exponentially greater transition rates are increased,^{3,4} and transitions at low bias can now proceed via these states. In device A, the FC gap is lifted at 3 K (Figure 4c,d), and device C at 4 K (Supporting Information Figure S8b,c). We extract and fit the temperature dependence of $I \propto 1/k_B T \times 1/(\exp(\hbar\omega/k_B T) - 1)$ ^{3,4} at $V_g = 7$ V and $V_b = 7.2$ mV in Figure 4c and obtained a value of $\hbar\omega = 1.7$ meV (Supporting Information Figure S9), accordant with the value measured in Figure 3c. The increase of peak intensity with temperature is in direct contrast with the case for which a Fermi–Dirac distribution is relevant, where a decrease is expected, $I \propto 1/k_B T$.³ This observation confirms the bosonic nature of the transition and is consistent with our interpretation of the FC model.

There exist two ways in which mechanical and electron degrees of freedom can couple, either through internal molecular vibrations or through center-of-mass oscillations. Where internal vibrations couple directly to the charge degree of freedom, CM oscillations couple through displacement dependent tunneling matrix elements instead.²² For energies below 10 meV, the coupling strength for CM oscillations is predicted to be insufficient to induce FC blockade.⁴ In previous experiments, on pristine C_{60} single-molecules connected to gold electrodes no FC blockade was observed for low energy excitations (3 to 7 meV),² because these excitations are due to pure CM motion of the C_{60} . However, for the low energy excitation at 1.7 meV observed in our experiments the CM oscillation of the C_{60} is accompanied by an internal vibration of the combined C_{60} -pyrene system, as illustrated by the vibrational energy spectrum shown in Figure S15 and the

animations in the Supporting Information. Because electron–vibron coupling mediated by internal vibrations can be much stronger than electron–vibron coupling mediated by CM oscillations,⁴ we attribute the observation of FC blockade in our system to the internal vibrations of the functionalized C_{60} .

Strong electron–vibron coupling and weak vibron relaxation can further lead to avalanche transport characterized by strong current fluctuations.⁵ These fluctuations are the result of occasional charge transfer events exciting the molecule from its vibrational ground state and setting off an avalanche of electrons tunneling via vibrational excited states that have greater wave function overlap, as shown in Figure 5a–f. An avalanche is terminated when the molecule returns to its ground state by tunneling induced de-excitation or dissipative relaxation. Figure 5g shows that avalanche transport, in contrast to field-induced bistabilities,²³ leads to fluctuations that persist over the entire bias range corresponding to the vibrational $0 \leftrightarrow 2$ transition. For $\beta eV_b < 2\hbar\omega$ ($\beta \sim 0.5$ given by the ratio of the source capacitance and the total capacitance), the vibrational transitions $0 \leftrightarrow 0$ and $0 \leftrightarrow 1$ are suppressed due to FC blockade (Figure 5a,d). At $2\hbar\omega \leq \beta eV_b < 3\hbar\omega$, the $0 \leftrightarrow 2$ transition enters the bias window (Figure 5b,e). While the transition rate is higher, the system typically experiences a long wait time with no current while it remains in the vibron ground state. For weak vibron relaxation, occasional electron inelastic tunnelling excites the molecule to a higher vibrational state with subsequent tunnelling events further increasing this excitation. Having escaped the ground state, an avalanche of tunnelling events occur. The process terminates when the system returns to the vibrational ground state, resulting in another long wait time before the cycle repeats. At $\beta eV_b \geq 3\hbar\omega$, charge transfer proceeds via sequential tunnelling through the $0 \leftrightarrow 3$ transition (Figure 5c,f).

To characterize the current fluctuations, we extract the $0 \leftrightarrow 2$ escape and return rates by fitting a current–time trace of device A measured at $V_b = 12$ mV and $V_g = 10.15$ V to a Hidden Markov Model (HMM) assuming a two state stochastic process (orange line in Figure 5e).²⁴ We obtain an escape rate of 15 ± 2 s⁻¹, which corresponds to a FC matrix element $W_{0 \leftrightarrow 2} \sim 0.002$ and $\lambda \sim 4$ (Supporting Information Section 1.9), and a return rate of 22 ± 2 s⁻¹. These rates place an upper-bound of ~ 10 s⁻¹ on the dissipative relaxation rate. The observation of such a slow relaxation rate, compared to values measured in time-resolved spectroscopy (~ 1 ps⁻¹),²⁵ is indeed surprising. However, those measurements are usually performed in a solvent where dissipation to solvent ions is possible. Low temperature and vacuum conditions suppresses the dissipation rate,²⁶ which is mostly dependent on dissipation to the electrodes in single-molecule junctions.^{10,27} Fits of the conductance peaks (Supporting Information Section 1.5) show that the pyrene anchors form weak π – π stacking interactions with the graphene electrode (molecule–electrode coupling $t_0 \sim 1$ meV). While the in-plane thermal conductivity of graphene is exceptionally large, its out-of-plane thermal conductivity is limited by weak van der Waals interactions between adjacent planes and substrates and can possibly suppress vibron dissipation to the graphene electrodes.²⁸ Vibrationally induced conformational changes where an anharmonic potential with local minimas suppress dissipation is another possibility.¹ Metastable molecular conformation can be long-lived on the order of milliseconds, consistent with the return rates in our system, and can be accessed through a vibrational excited state.²⁹ Dissipation to the electrodes is

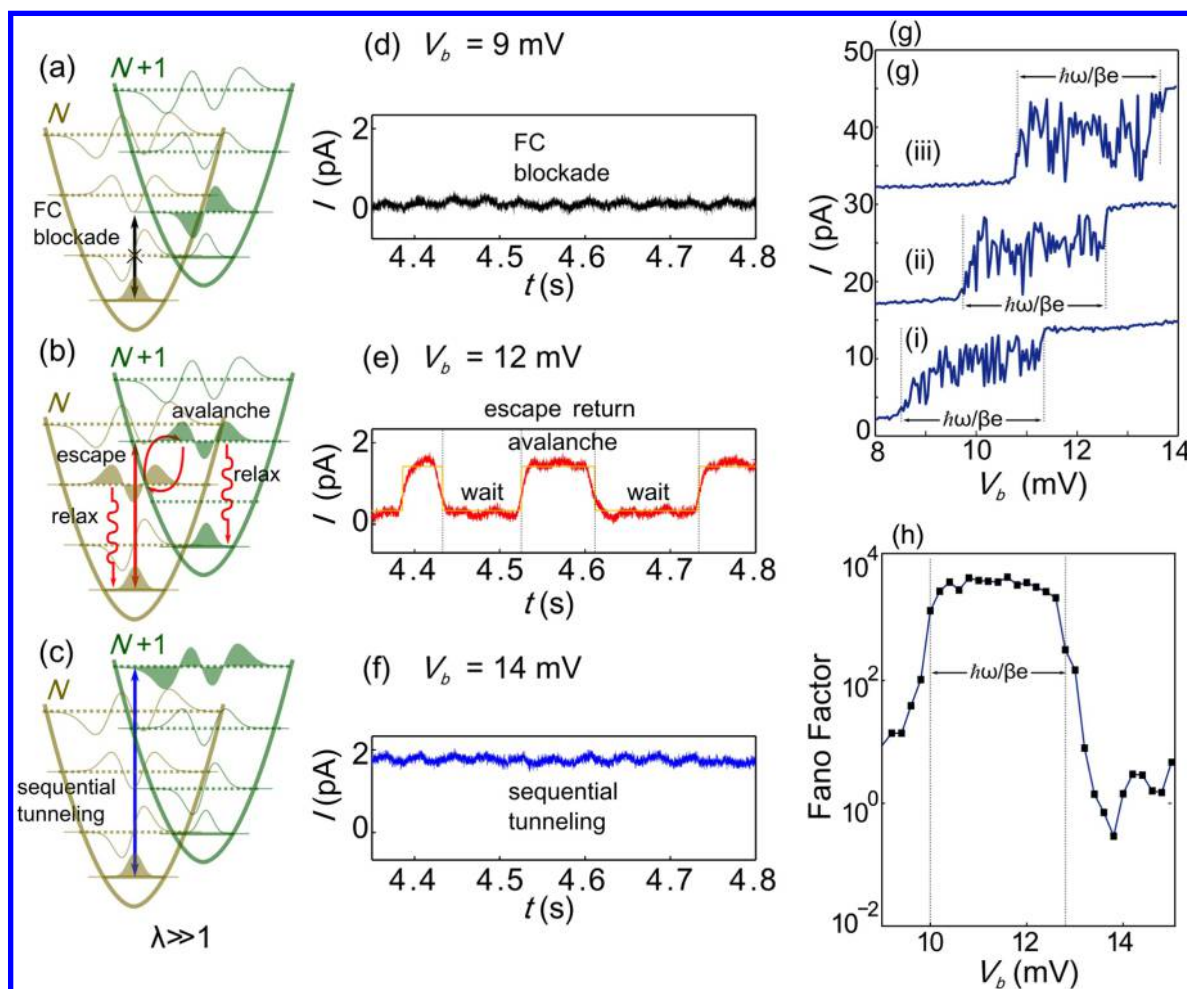


Figure 5. (a–c) Schematics for avalanche transport. (d–f) Current–time traces at $V_b = 9, 12,$ and 14 mV and $V_g = 10.15$ V. The full current–time trace over which we perform the HMM fit was measured for 20 s with a 100 kHz sampling rate. The orange curve (e) is the HMM fit to the full current–time trace. (g) I – V traces at $V_g =$ (i) 10.1, (ii) 10.15, and (iii) 10.2 V. Curves are offset for clarity, +15 (ii) and +30 pA (iii). The current noise extends over an applied bias corresponding to $\hbar\omega/\beta e$. (h) Fano factors of the zero-frequency noise measured as a function of V_b at $V_g = 10.15$ V as indicated by the green line in Figure 3c. Giant Fano factors $\sim 10^3$ extend over an applied bias corresponding to $\hbar\omega/\beta e$, reflecting avalanche transport, before decreasing to ~ 1 at higher bias in accordance with sequential tunnelling.

dependent on the atomistic details of the vibron density of states at the molecule–electrode interface. The nonequilibrium distribution of vibrons is nontrivial and requires a self-consistent calculation of electron–vibron dynamics.

Electron avalanche transport is characterized by giant Fano factors on the order of 10^2 – 10^3 occurring in steps over the bias window ($\hbar\omega/\beta e$) corresponding to a vibron transition.⁵ The zero frequency Fano factor $F = S/2e\langle I \rangle$ for the excess noise $S(0) - S(0)_{V_b=0}$ indicates the deviation from Poissonian noise, where $F = 1$. The noise power density $S(\omega)$ is defined as the Fourier transform of the current–current correlation

$$S(\omega) = \int_{-\infty}^{\infty} dt e^{i\omega t} \langle \delta I(t + t') \delta I(t') \rangle_t \quad (1)$$

In Figure 5h, we determine the zero frequency Fano factors as a function of V_b (Supporting Information Section 1.9), taken at $V_g = 10.15$ V indicated by the vertical green line in Figure 3c. At $10 \leq V_b \leq 13$ mV, the Fano factors increase to an order of $\sim 10^2 - 10^3$, reflecting the current fluctuations due to avalanche transport. These giant Fano factors likewise persist over an applied bias corresponding to $\hbar\omega$. When V_b is sufficient to lift FC blockade, the Fano factor is expected to return to values of

the order of 1.⁵ At $V_b = 13.4$ mV, the Fano factors decrease to ~ 1 in accordance with sequential transport.³⁰

We have demonstrated a device architecture, using functionalized C_{60} bisadduct and graphene electrodes to create single-molecule transistors, that enables the observation of redox-dependent FC blockade and avalanche transport. We observe HOMO dominated transport.¹⁰ While doping-induced variations in the Fermi-level of the graphene electrodes and offset charges in the oxide can influence the alignment of the electrochemical potential of the molecule with the Fermi-level of the graphene electrodes, we show that the functionalization of C_{60} with pyrene anchors groups can modify electron delocalization and energy levels leading to HOMO dominated transport, which is in contrast to previous reports of LUMO dominated transport in C_{60} transistors. Calculations have suggested that the modification of electron delocalization and energies via the inclusion of side groups can be used to tune the thermopower of single-molecule junctions.^{31,32} Furthermore, thermoelectric efficiency is maximized when charge transport across a junction occurs through a single level with low vibrational heat conductance.³² Therefore, the observation of an extremely long vibron lifetime not only offers unique

potential for the fundamental study of quantized motion and thermal transport on the nanoscale but is also promising for practical applications in single-molecule energy-conversion devices.³²

Methods. Device Fabrication and Measurements. The molecular devices are fabricated on a heavily doped silicon chip with a 300 nm thick oxide that also serves as a back gate to modulate charge transport through the junction. First, graphene is synthesized on liquid copper supported on a tungsten substrate using chemical vapor deposition.³³ Using a wet transfer technique, the graphene is transferred to the silicon substrate with prepatterned gold electrodes. The graphene electrodes are fabricated based on the method of feedback-controlled electroburning.³⁴ Fabricated nanogaps are typically between 1 to 2 nm. The devices are next immersed in a 10 μ M chloroform solution containing the C₆₀ bisadducts for 30 min. We wirebond the devices to our sample puck and transfer them to our dilution fridge with a base temperature of 20 mK. All electrical measurements are performed using low noise, battery operated electronics, while the gate voltage was modulated with a Keithley 2400 sourcemeter.

Theoretical Methods. To calculate the vibrational modes of the bisadducts, we use the Harmonic approximation method to construct the Dynamical Matrix *D*. The *xyz* coordinates of the two isomers of the bisadducts were constructed and the geometry relaxation was performed with Siesta³⁵ implementation of the DFT by double- ζ polarized bases set and the generalized gradient approximation functional with Perdew–Burke–Ernzerhof parametrization to the force tolerance of 20 meV/Å. A real-space grid is defined with an equivalent energy cutoff of 250 Ry. From the relaxed *xyz* coordinates of the system, a set of the *xyz* coordinates were generated by displacing each atom in positive and negative *x*, *y*, and *z* directions by $\delta q' = 0.01$ Å. The forces in three directions $q_i = (x_i, y_i, z_i)$ on each atom were then calculated by DFT with the same parameters as the relaxed system but without geometry relaxation. These set of the force $F_i^q = (F_i^x, F_i^y, F_i^z)$ vectors are used to construct the dynamical matrix (Supporting Information Section 2.1).³⁶ The electronic structure and transport calculations are performed using GOLLUM as described in ref 8.

■ ASSOCIATED CONTENT

● Supporting Information

The Supporting Information is available free of charge on the ACS Publications website at DOI: 10.1021/acs.nanolett.5b03434.

Further details about molecular synthesis and characterization, magnetic and temperature dependence measurements, rate equation model, current noise analysis, DFT calculations. (PDF)

Animations of the molecular vibrations. (ZIP)

■ AUTHOR INFORMATION

Corresponding Author

*E-mail: jan.mol@materials.ox.ac.uk. Phone: +44 1865 273719.

Notes

The authors declare no competing financial interest.

■ ACKNOWLEDGMENTS

We thank the Royal Society for a Newton International Fellowship for J.A.M. and a University Research Fellowship for

J. H.W., and the Agency for Science Technology and Research (A*STAR) for a studentship for C.S.L. This work is supported by Oxford Martin School, EPSRC Grants EP/J015067/1, EP/K001507/1, EP/J014753/1, EP/H035818/1, EP/K030108/1 and the European Union Marie-Curie Network MOLESCO. This project/publication was made possible through the support of a grant from Templeton World Charity Foundation. The opinions expressed in this publication are those of the author(s) and do not necessarily reflect the views of Templeton World Charity Foundation.

■ REFERENCES

- (1) Galperin, M.; Ratner, M. A.; Nitzan, A. *J. Phys.: Condens. Matter* **2007**, *19*, 103201.
- (2) Park, H.; Park, J.; Lim, A.; Anderson, E.; Alivisatos, A.; McEuen, P. *Nature* **2000**, *407*, 57–60.
- (3) Leturcq, R.; Stampfer, C.; Inderbitzin, K.; Durrer, L.; Hierold, C.; Mariani, E.; Schultz, M. G.; von Oppen, F.; Ensslin, K. *Nat. Phys.* **2009**, *5*, 327–331.
- (4) Burzuri, E.; Yamamoto, Y.; Warnock, M.; Zhong, X.; Park, K.; Cornia, A.; Van Der Zant, H. S. J. *Nano Lett.* **2014**, *14*, 3191–3196.
- (5) Koch, J.; Von Oppen, F. *Phys. Rev. Lett.* **2005**, *94*, 206804.
- (6) Mol, J. A.; Lau, C. S.; Lewis, W. J. M.; Sadeghi, H.; Roche, C.; Cnossen, A.; Warner, J. H.; Lambert, C. J.; Anderson, H. L.; Briggs, G. A. D. *Nanoscale* **2015**, *7*, 13181–13185.
- (7) Maggini, M.; Scorrano, G.; Prato, M. *J. Am. Chem. Soc.* **1993**, *115*, 9798–9799.
- (8) Sadeghi, H.; Mol, J. A.; Lau, C. S.; Briggs, G. A. D.; Warner, J.; Lambert, C. J. *Proc. Natl. Acad. Sci. U. S. A.* **2015**, *112*, 2658–2663.
- (9) Yee, S. K.; Malen, J. A.; Majumdar, A.; Segalman, R. A. *Nano Lett.* **2011**, *11*, 4089–4094.
- (10) Schulze, G.; Franke, K. J.; Gagliardi, A.; Romano, G.; Lin, C. S.; Rosa, A. L.; Niehaus, T. A.; Frauenheim, T.; Di Carlo, A.; Pecchia, A.; Pascual, J. I. *Phys. Rev. Lett.* **2008**, *100*, 136801.
- (11) Al-Galiby, Q.; Grace, I.; Sadeghi, H.; Lambert, C. J. *J. Mater. Chem. C* **2015**, *3*, 2101–2106.
- (12) Kubatkin, S.; Danilov, A.; Hjort, M.; Cornil, J.; Brédas, J.-L.; Stühr-Hansen, N.; Hedegård, P.; Bjørnholm, T. *Nature* **2003**, *425*, 698–701.
- (13) Ke, S.-H.; Baranger, H.; Yang, W. *Phys. Rev. Lett.* **2003**, *91*, 116803.
- (14) Kaasbjerg, K.; Flensberg, K. *Nano Lett.* **2008**, *8*, 3809–14.
- (15) Heid, R.; Pintschovius, L.; Godard, J. M. *Phys. Rev. B: Condens. Matter Mater. Phys.* **1997**, *56*, 5925–5936.
- (16) Lansbergen, G. P.; Rahman, R.; Verduijn, J.; Tettamanzi, G. C.; Collaert, N.; Biesemans, S.; Klimeck, G.; Hollenberg, L. C. L.; Rogge, S. *Phys. Rev. Lett.* **2011**, *107*, 136602.
- (17) Fuechle, M.; Miwa, J. a.; Mahapatra, S.; Ryu, H.; Lee, S.; Warschkow, O.; Hollenberg, L. C. L.; Klimeck, G.; Simmons, M. Y. *Nat. Nanotechnol.* **2012**, *7*, 242–246.
- (18) Bailey, S.; Visontai, D.; Lambert, C. J.; Bryce, M. R.; Frampton, H.; Chappell, D. *J. Chem. Phys.* **2014**, *140*, 054708.
- (19) Winkelmann, C. B.; Roch, N.; Wernsdorfer, W.; Bouchiat, V.; Balestro, F. *Nat. Phys.* **2009**, *5*, 876–879.
- (20) Lannoo, M.; Baraff, G. A.; Schlüter, M.; Tomanek, D. *Phys. Rev. B: Condens. Matter Mater. Phys.* **1991**, *44*, 12106–12108.
- (21) O'Brien, M. C. M. *Am. J. Phys.* **1993**, *61*, 688.
- (22) Koch, J.; Von Oppen, F.; Oreg, Y.; Sela, E. *Phys. Rev. B: Condens. Matter Mater. Phys.* **2004**, *70*, 1–12.
- (23) Secker, D.; Wagner, S.; Ballmann, S.; Härtle, R.; Thoss, M.; Weber, H. B. *Phys. Rev. Lett.* **2011**, *106*, 3–6.
- (24) Greenfeld, M.; Pavlichin, D. S.; Mabuchi, H.; Herschlag, D. *PLoS One* **2012**, *7*, e30024.
- (25) Laubereau, A.; von der Linde, D.; Kaiser, W. *Phys. Rev. Lett.* **1972**, *28*, 1162–1165.
- (26) Kuznetsov, A. M.; Ulstrup, J. *J. Electroanal. Chem.* **2004**, *564*, 209–222.

- (27) Pascual, K. J. F.; Ignacio, J. *J. Phys.: Condens. Matter* **2012**, *24*, 394002.
- (28) Pop, E.; Varshney, V.; Roy, A. K. *MRS Bull.* **2012**, *37*, 1273–1281.
- (29) Eggeling, C.; Fries, J. R.; Brand, L.; Günther, R.; Seidel, C. A. M. *Proc. Natl. Acad. Sci. U. S. A.* **1998**, *95*, 1556–1561.
- (30) Onac, E.; Balestro, F.; Trauzettel, B.; Lodewijk, C.; Kouwenhoven, L. *Phys. Rev. Lett.* **2006**, *96*, 026803.
- (31) Kim, Y.; Jeong, W.; Kim, K.; Lee, W.; Reddy, P. *Nat. Nanotechnol.* **2014**, *9*, 881–885.
- (32) Reddy, P.; Jang, S.-Y.; Segalman, R. A.; Majumdar, A. *Science* **2007**, *315*, 1568–1571.
- (33) Wu, Y. a.; Fan, Y.; Speller, S.; Creeth, G. L.; Sadowski, J. T.; He, K.; Robertson, A. W.; Allen, C. S.; Warner, J. H. *ACS Nano* **2012**, *6*, 5010–7.
- (34) Lau, C. S.; Mol, J. A.; Warner, J. H.; Briggs, G. A. D. *Phys. Chem. Chem. Phys.* **2014**, *16*, 20398–401.
- (35) Soler, J. M.; Artacho, E.; Gale, J. D.; García, A.; Junquera, J.; Ordejón, P.; Sánchez-Portal, D. *J. Phys.: Condens. Matter* **2002**, *14*, 2745.
- (36) Sadeghi, H.; Sangtarash, S.; Lambert, C. J. *Nano Lett.* **2015**, *15*, 7467–7472.